
Article:
Huang, X., Hunter, C.N. orcid.org/0000-0003-2533-9783 and Vasilev, C. orcid.org/0000-0002-0536-882X (2021) Multicomponent nanoscale patterning of functional light-harvesting protein complexes by local oxidation lithography. Advanced Materials Interfaces, 8 (5). 2001670. ISSN 2196-7350

https://doi.org/10.1002/admi.202001670

ADVANCED MATERIALS INTERFACES
www.advmatinterfaces.de

Multicomponent Nanoscale Patterning of Functional Light-Harvesting Protein Complexes by Local Oxidation Lithography

*Xia Huang, Christopher Neil Hunter, and Cvetelin Vasilev**

Local oxidation lithography has the potential for patterning proteins on conductive substrates such as silicon with nanometer accuracy, guided by and extending the nanoscale architectures found in native bioenergetic membranes. Such membranes foster energy and electron transfers between two or more types of protein complex, so the potential of this lithographic technique is investigated for copatterning multiple types of protein complex. Composite patterns consisting of light-harvesting 2 (LH2) and reaction center-light-harvesting 1-PufX (RCLH1) complexes purified from *Rhodobacter (Rba.) sphaeroides*, and light-harvesting complex II (LHCII) purified from spinach, are fabricated. Atomic force microscopy (AFM) images demonstrate the successful sequential deposition of single-molecule layers of RCLH1 and LH2 molecules. In the case of LHCII, a mixture of single-layer and multilayer patterns is found on the silicon substrate. Experimental conditions are established for the most efficient substrate surface modification and for protein immobilization. Spectral imaging and fluorescence lifetime imaging microscopy (FLIM) show that the immobilized photosynthetic complexes retain their native light-harvesting and energy transfer functions, and provide evidence for excitation energy transfer from LH2 to RCLH1. Local oxidation lithography has the capacity to pattern proteins singly, or in small domains, for fabricating bioinspired nanoscale architectures for biosensors and solar cells.

1. Introduction

In bacterial and plant photosynthesis, sunlight harvested by (bacterio)chlorophyll–protein complexes migrates as excited states (excitons) through a network of light-harvesting antenna complexes, until it arrives at the specialized complexes, reaction centers (RCs), where charge separation takes place and the excitation energy is converted into a stable charge separation.[1–3] In photosynthetic bacteria, light harvesting and energy transfer occur in a system of intracytoplasmic membranes (ICM), which in the case of *Rhodobacter (Rba.) sphaeroides* take the form of vesicles, generally 50–60 nm in diameter.[4,5] The processes of energy transfer and trapping take ≈65 ps with a quantum efficiency of ≈95%.[6,7] Exploiting these characteristics of antenna and reaction center complexes, in terms of highly efficient energy-transfer and charge-separation processes, is a major goal in producing bioinspired photovoltaic cells. Developing procedures for controlling the distribution of light-harvesting antennas and reaction centers on the nanoscale, while retaining their functionality on conductive substrates, is an important step toward this goal.

Substrates such as gold and glass are widely used for the immobilization of proteins. The surface properties of these substrates are generally modified by physical or chemical means to control the attachment of the target molecule. Self-assembled monolayers (SAMs), as the most extensively studied method, are generally used in modifying gold, silicon, and glass substrates.[8–11] SAMs have been applied to study the attachment of a variety of biological materials. Photosynthetic complexes have previously been attached to insulating substrates such as glass,[12–14] and conductive substrates such as gold,[15–17] and indium–tin oxide (ITO).[18] These studies demonstrated that immobilized photosynthetic complexes retained their functional properties. A similar immobilization approach allows measurements of the photocurrent resulting from immobilized charge-separating reaction centers onto conductive surfaces.[15,19–21] However, such studies generally do not control the distribution of the reaction centers on the underlying surfaces, either laterally or in terms of the numbers of layers deposited. Developments in nanofabrication techniques make it possible to create nanometer scale molecular assemblies and direct the distribution of single layers of protein complexes.[22] These techniques include photolithography,[16,17,23–25] dip-pen nanolithography (DPN),[26–29]

Dr. X. Huang
Suzhou Institute of Biomedical Engineering and Technology
Chinese Academy of Sciences
Keling Road, Suzhou, Jiangsu Province 215163, China
Dr. X. Huang, Prof. C. N. Hunter, Dr. C. Vasilev
Department of Molecular Biology and Biotechnology
University of Sheffield
Sheffield S10 2TN, UK
E-mail: c.vasilev@sheffield.ac.uk
The ORCID identification number(s) for the author(s) of this article can be found under https://doi.org/10.1002/admi.202001670.

DOI: 10.1002/admi.202001670

nanoimprint lithography (NIL),[12–14,30] scanning near-field photolithography (SNP),[31–33] and local oxidation lithography.[34–37] However, most of the efforts in nanopatterning of photosynthetic complexes have been focused on attaching a single type of complex such as light-harvesting 2 (LH2), reaction center-light-harvesting 1-PufX (RCLH1), or light-harvesting complex II (LHCII) to a surface, and it was only very recently that we demonstrated excitation energy transfer between intersecting lines of LH2 and RCLH1 patterned sequentially onto glass substrate with a spatial distribution controlled on a micrometer rather than a nanometer scale.[38]

In this work, we have created composite nanoarrays containing LHCII, LH2, and RCLH1 photosynthetic complexes arranged with nanometer accuracy on chemically functionalized silicon substrates with methyl-terminated polyethylene glycol SAMs (mPEG-SAM) modified by local oxidation lithography. This approach provides greater flexibility in designing protein nanoarrays with specific geometries and composition compared to other recently developed nanopatterning methods. By varying the experimental conditions, we were able to find the most efficient protocol for oxidizing the silicon surface and for attaching proteins. The resulting multiprotein nanoarrays were studied by atomic force microscopy (AFM) and fluorescence microscopy. Our results confirmed that the photosynthetic complexes retained their structural and optical properties after surface immobilization. By performing two successive local oxidation patterning steps, we have created composite patterns consisting of LH2 and RCLH1 complexes in very close proximity, similar to their arrangement in the intracytoplasmic membrane. Energy transfer between the patterned LH2 and RCLH1 complexes was studied by monitoring the fluorescence lifetime of the LH2 complexes. This work establishes a method for patterning multiple types of protein complexes on a conductive surface with their distribution controlled on a nanometer scale while preserving protein functionality. Our approach paves the way to fabricate conductive biochips for light-harvesting and charge-separation purposes, and it represents a useful step forward for producing bioinspired nanoscale architectures for biosensors and solar cells.

2. Results and Discussion

2.1. Nanopatterning of Photosynthetic Complexes by Local Oxidation Lithography on an mPEG-Functionalized Silicon Surface

A schematic representation of the local oxidation lithography process used for nanopatterning photosynthetic complexes on an mPEG-functionalized silicon surface is shown in **Figure 1**A. By scanning a conductive AFM probe with a bias applied between the substrate surface and the AFM probe, the mPEG monolayer was locally oxidized by the current passing through the water meniscus formed between the tip and the silicon surface. The terminal $-CH_3$ groups on the mPEG-SAM were oxidized to −COOH groups,[35,39–41] while at the same time the thickness of the underlying silicon oxide layer increased (due to the oxidation of the substrate).[42,43] The −COOH groups were subsequently reacted with an aqueous solution of 1-ethyl-3-[3-dimethylaminopropyl] carbodiimide hydrochloride (EDC) and *N*-hydroxysuccinimide (NHS) to form NHS-ester groups over the oxidized parts of the monolayer. The photosynthetic complexes were then selectively crosslinked via ester-to-lysine bonds to form protein nanopatterns (**Figure 2**C), while the nonoxidized mPEG areas provide protein-resistant background. Repeating the process over the same area with a different orientation of the raster scan allows the creation of multiprotein nanopatterns (Figure 1B).

First, we used lateral force microscopy (LFM) to investigate the surface nanopatterns produced by oxidizing the mPEG-SAM deposited on the silicon substrate. The contrast in the surface lateral force arises from the change in the surface chemistry ($-CH_3$ to −COOH groups), while the surface topography is altered due to the oxidation of the underlying silicon substrate to silicon oxide. Figure 2A,B shows an AFM topographic image and an AFM lateral force image of locally oxidized mPEG-SAM, respectively. During the local oxidation process, the AFM probe scanned the sample surface at a constant velocity resulting in a pixel dwell time of around 100 ms. Four lines were drawn on the surface with the bias varied from 6 to

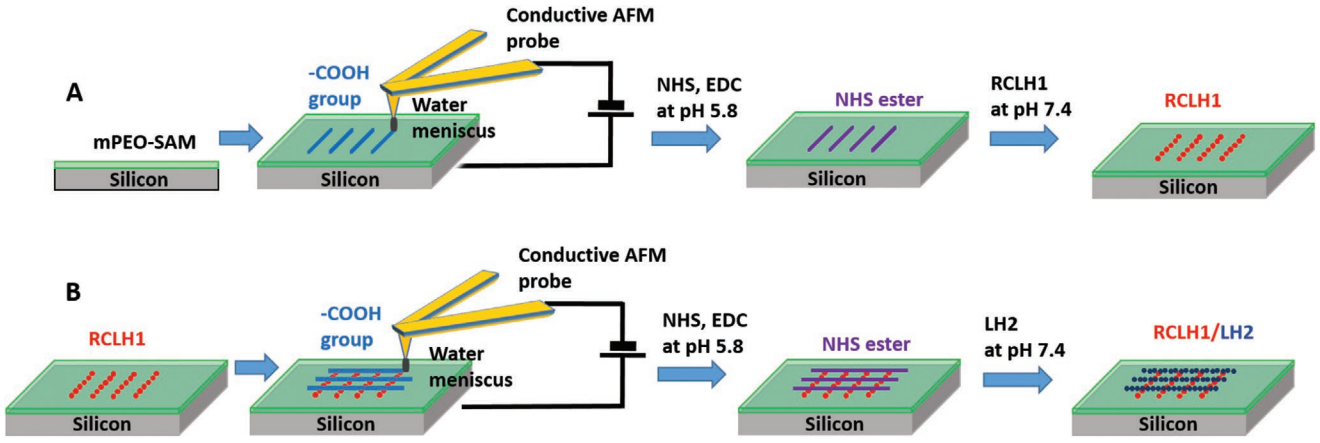

Figure 1. Schematic diagram of the local oxidation process and the subsequent protein immobilization. A) The local oxidation process forms four nanolines of oxidized mPEG monolayer functionalized with a crosslinker and enables subsequent immobilization of RCLH1 protein complexes. B) A subsequent orthogonal pattern of local oxidation over the same area, followed by attachment of LH2 complexes, yields a multiprotein nanoarray.

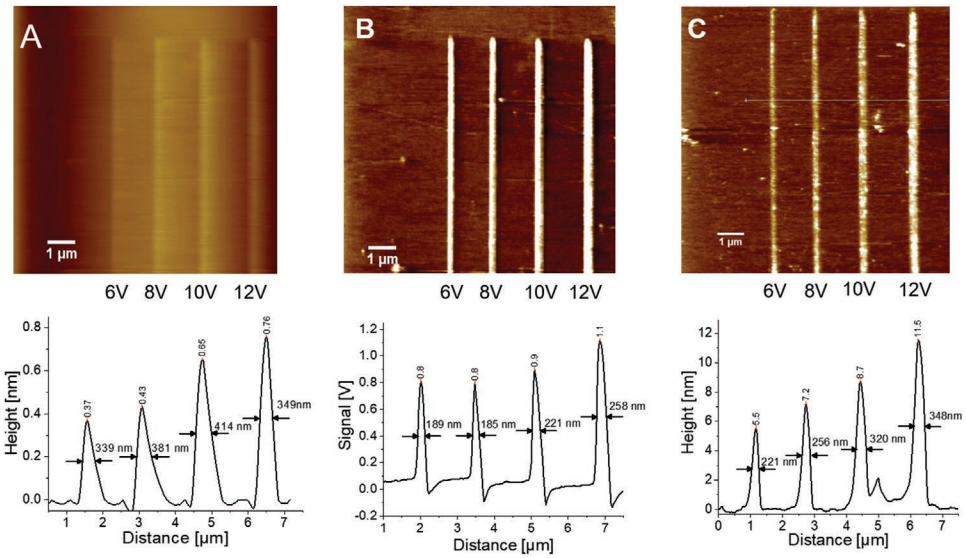

Figure 2. AFM characterization of RCLH1 complexes immobilized onto nanolines formed by local oxidation of mPEG. A) Topographic image of the −COOH nanolines on the mPEG-SAM-coated silicon surface (with the average height and FWHM of each line plotted) and B) the corresponding lateral force image of the same nanopattern (with the average relative lateral force variation of each line plotted). C) Topographic image of the immobilized RCLH1 complexes, with the average height and FWHM of each line plotted.

12 V. As evident from Figure 2A, higher bias voltage resulted in greater topographic changes—the average height of each subsequent nanoline increased from 0.37 to 0.76 nm, and the full width half maximum (FWHM) of the lines broadened from 339 to 414 nm. Surface lateral force contrast (Figure 2B) reveals that the brighter contrast (stronger interaction with the AFM probe) corresponds to the modified regions terminated with −COOH groups. The average lateral force amplitude and FWHM of each carboxyl-terminated nanoline increased from 0.8 to 1.1 V and from 185 to 258 nm, respectively, while ramping up the bias.

After NHS/EDC activation of the carboxyl groups, RCLH1 complexes were incubated on the sample surface for 6 h and then the surface distribution of the protein complexes was recorded under near-physiological conditions (in imaging buffer) by imaging the same area of the sample. The resulting average height of each nanoline (patterned at different probe–sample biases) with RCLH1 complexes attached increased from 5.5 to 11.5 nm and the average FWHM from 221 to 348 nm, as shown in Figure 2C. The RCLH1 complex is a disk-shaped dimeric transmembrane protein with each monomer having a diameter of around 11 nm and an overall height of around 9 nm.[44,45] Thus, the measured average heights for the two nanolines patterned at higher bias, 8.7 and 11.5 nm, respectively, are consistent with the expected RCLH1 height. The lower average height and the smaller average FWHM indicate that a lower bias voltage results in less efficient mPEG oxidation, which leads to a lower RCLH1 occupancy.

Active lysine residues are present both on the periplasmic and cytoplasmic sides of the protein complex resulting in a bimodal orientation of the proteins on the substrate (periplasmic side facing up or down). In addition, the RCLH1 complex has a natural tendency to form dimers; however, the semiaerobic growth conditions used in this work result in an increased proportion of monomers.[46] Hence, we expect a mixture of monomers and dimers immobilized on the substrate. However, this does not affect the measured heights of the RCLH1 nanopatterns, as both the dimers and monomers have the same height.

2.2. Optimization of mPEG Oxidation and Protein Immobilization

To fabricate nanopatterns with a high protein occupancy, we investigated a range of experimental conditions for more effective mPEG oxidation and better protein immobilization. **Figure 3**A shows false color fluorescence images of RCLH1 nanolines fabricated by varying the local oxidation parameters. After the oxidation step, all the samples were incubated with RCLH1 complexes for 6 h. Each group of nanolines was created using the same probe scanning velocity and probe–sample bias voltage varying in the range of 6–12 V. Quantifying the total fluorescence intensity from each RCLH1 nanoline, Figure 3B, reveals that longer pixel dwell time (lower probe velocity) and higher bias voltage generally lead to increased fluorescence intensity from the nanolines, thus indicating a higher RCLH1 occupancy. The RCLH1 nanoline with the highest fluorescence intensity (best occupancy) was fabricated at a bias of 12 V and a pixel dwell time of 100 ms (indicated with a white rectangle in Figure 3A). The fluorescence emission spectrum recorded from this RCLH1 nanoline matched very well with the spectrum of solubilized RCLH1 complexes (20×10^{-3} M 4-(2-hydroxyethyl)-1-piperazineethanesulfonic acid (HEPES), pH 7.8, 0.03% *n*-dodecyl β-D-maltoside (β-DDM)), Figure 3C, indicating that the surface-immobilized complexes retained their structural and optical properties after the nanopatterning process.

As a next optimization step, the probe–sample bias voltage was fixed at 12 V, and the pixel dwell time was deliberately prolonged from 80 to 240 ms pixel^{-1}, but no consistent increase in RCLH1 fluorescence intensity was observed when bias duration

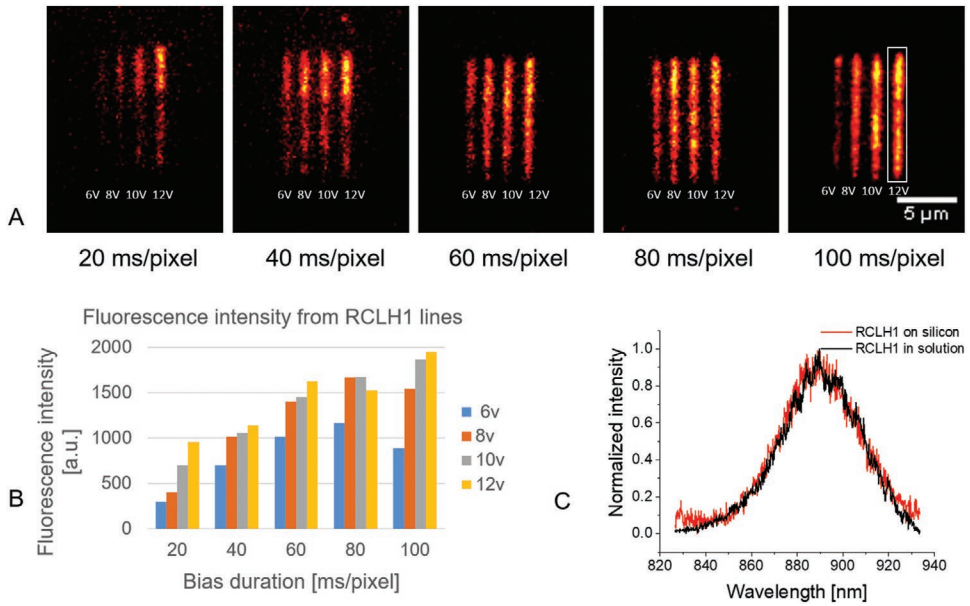

Figure 3. Fluorescence emission characterization of the nanopatterned RCLH1 complexes. A) False color fluorescence images of the RCLH1 nanolines, excitation at 470 nm, fluorescence emission recorded through a 900/32 nm bandpass filter. B) Quantified fluorescence intensity of each of the RCLH1 nanolines in panel (A). C) Comparison between the emission spectra of RCLH1 complexes immobilized onto the nanolines and in solution, both excited at 470 nm.

was more than 100 ms pixel^{-1} (Figure S1, Supporting Information). Following efficient mPEG oxidation, the protein incubation time was also tested, where the RCLH1 complexes were incubated on the sample surface at 4 °C from 40 min to 20 h. The result showed that a 4 h incubation yielded the maximum RCLH1 fluorescence intensity (Figure S2, Supporting Information). Therefore, a bias of 12 V, a pixel dwell time of 100 ms, and an incubation time of 4 h were chosen as the standard experimental condition for subsequent experiments.

By using the same experimental conditions, we successfully created linear nanopatterns of LH2 protein complexes as shown in **Figure 4**. The AFM of a nanoline of LH2 complexes (Figure 4A, inset) showed that they are densely packed, mimicking the arrangement in native membranes.[47,48] Analysis of the AFM topography image taken after the protein immobilization (Figure 4A) revealed an average nanopattern height of around 6 nm (Figure 4B). LH2 is a ring-shaped transmembrane protein with a diameter of ≈6 nm and a height of 6 nm.[49,50] Therefore, the measured heights are in a good agreement with the expected height of the LH2 protein complex derived from its structure. The LH2 protein has a somewhat well-defined sidedness with the majority of the lysine residues on the periplasmic side of the complex. Thus, we are expecting that majority of the LH2 complexes immobilized on the substrate are attached with the periplasmic side facing the substrate. The fluorescence emission spectrum in Figure 4C acquired from an LH2 nanoline matched well with the spectrum from solubilized LH2 complexes in buffer (20×10^{-3} M HEPES, pH 7.8, 0.03% β-DDM). This is a clear indication that the LH2 complexes retained their structural and optical properties after immobilization on the silicon surface.

Following the same protocol, we were able to create nanopatterns of the LHCII, the major light absorber in plants. The characterization of the topology of these samples showed that the resulting nanolines had somewhat irregular height with numerous large protein aggregates immobilized along the lines (**Figure 5**A,B). LHCII is a trimeric transmembrane protein complex with a height of around 5.5 nm,[51,52] and the measured average heights of the LHCII nanolones, 5.3 and 7.6 nm, are consistent with the expected height of the LHCII complex (taking into account the possible aggregation). LHCII exhibits an *N*-terminal (chloroplast stroma-facing) side that is particularly enriched of lysine residues, and we expect a fairly uniform orientation of the complex on the surface. The fluorescence emission spectrum of the nanopatterned LHCII matches very well with the spectrum of solubilized LHCII in buffer (20×10^{-3} M HEPES, pH 7.8, 0.03% β-DDM) (Figure 5C), indicating that the LHCII complexes also retained their structure and functionality after the surface immobilization.

It is worth noting that the nanopatterned protein complexes lie in close proximity to the underlying semiconductor substrate, separated only by the native oxide layer (typically around 2.5 nm thick plus a small increase in thickness due to the local oxidation). The energy of the fluorescence emission from either the three protein complexes exceeds the bandgap energy of the substrate (1.12 eV for Si), so there is significant absorption in the far-red to near-infrared range, where all three protein molecules emit. This absorption can lead to nonradiative transfer of excitation energy, exciting an electron from the valence band to the conduction band of the semiconductor. This energy-transfer process occurs via a dipole-induced mechanism, similar to Förster energy transfer,[53,54] and leads to a dramatic quenching of the fluorescence emission from the light-harvesting protein complexes.

Despite the weak fluorescence emission from the surface-quenched light-harvesting complexes, we were able to acquire

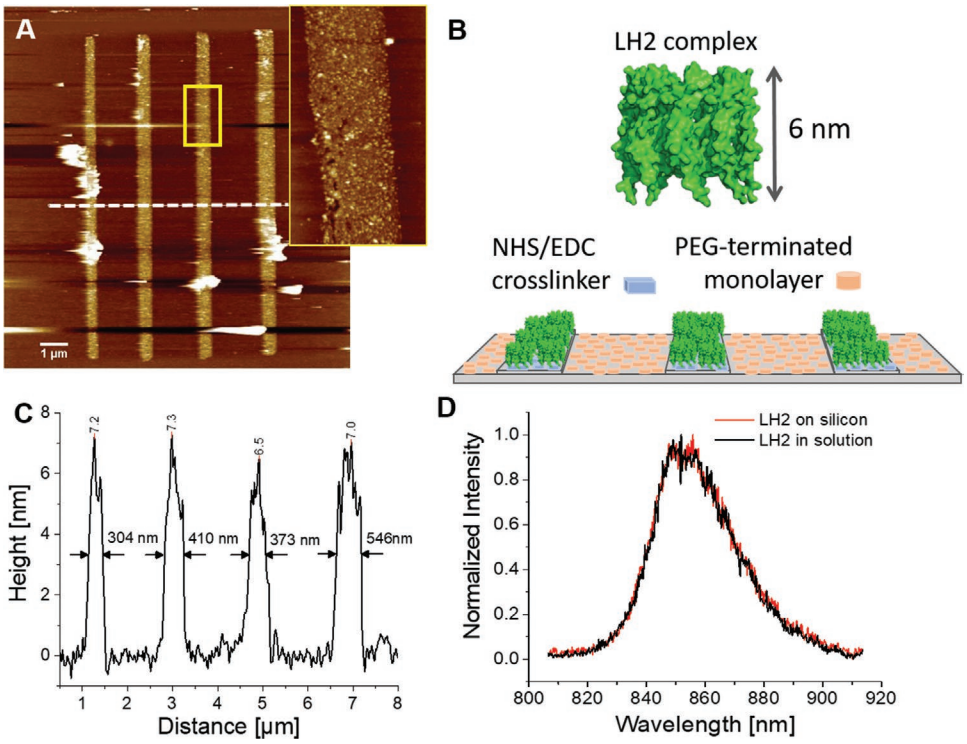

Figure 4. AFM and fluorescence emission characterization of nanopatterned LH2 complexes on functionalized silicone substrate. A) Topographic image of the LH2 nanolines on the mPEG-SAM-coated silicon surface. The topography of one of the nanolines (yellow rectangle) is shown in greater detail as an inset. B) Schematic representation of the surface-immobilized LH2 protein complexes on the surface with an inset showing the side view of the complex and its approximate height. C) A cross section along the dashed line in panel (A) showing the height and FWHM of each line. D) Comparison between the emission spectra of LH2 complexes immobilized onto the nanolines and in solution, both excited at 470 nm.

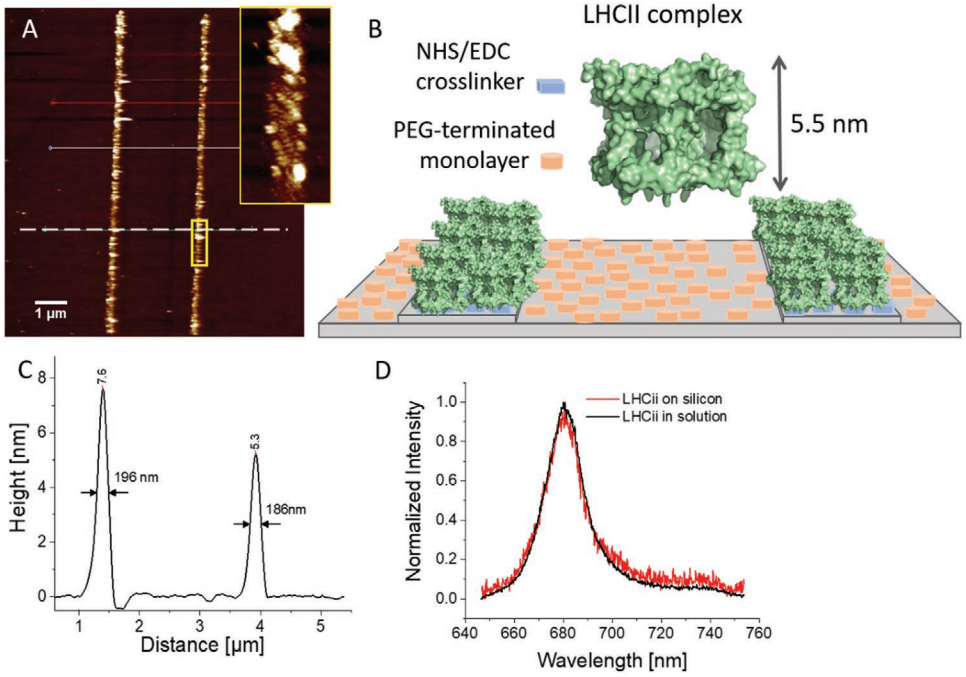

Figure 5. AFM and fluorescence emission characterization of nanopatterned LHCII complexes on functionalized silicone substrate. A) Topographic image of a pair of LHCII nanolines on the mPEG-SAM-coated silicon surface. The topography of one of the nanolines (yellow rectangle) is shown in greater detail as an inset. B) Schematic representation of the surface-immobilized LHCII protein complexes on the surface with an inset showing the side view of the complex and its approximate height. C) A cross section along the dashed line in panel (A) showing the height and FWHM of each line. D) Comparison between the emission spectra of LHCII complexes immobilized onto the nanolines and in solution (excitation at 470 nm).

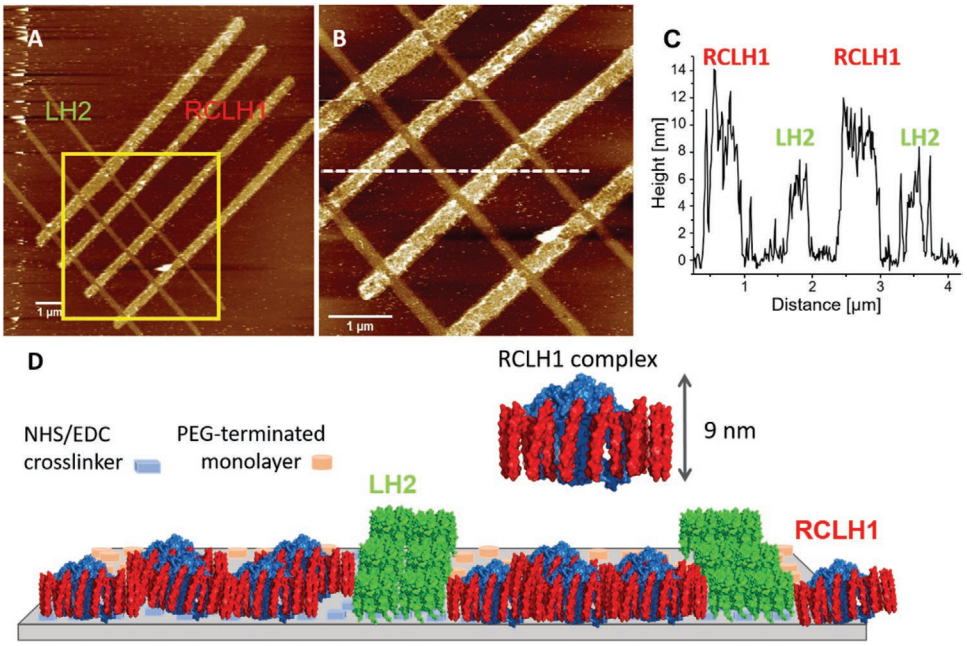

Figure 6. AFM topography of intersecting RCLH1 and LH2 nanolines created by successive nanopatterning over the same area on the substrate. A) Topographic image of a mixed LH2/RCLH1 nanopattern created by two-step local oxidation lithography B) with a higher resolution zoom-in corresponding to the yellow rectangle in panel (A). C) Height profile along the white dashed line in panel (B) showing heights of the LH2 and RCLH1 lines of ≈7 nm and ≈10 nm, respectively. D) Schematic representation of the surface-immobilized LH2 (green) and RCLH1 protein complexes (red/blue) on the surface with an inset showing the side view of the RCLH1 complex and its approximate height.

fluorescence emission data (images and spectra) of the nanopatterned proteins by increasing the electron multiplication gain on our charge-coupled device (CCD) detector as well as using relatively long exposure times. The obtained florescence data allowed us to conclude that all three types of light-harvesting proteins retained their structure, functionality, and optical properties after surface nanopatterning.

2.3. Co-Patterning of Two Types of Photosynthetic Protein Complexes by Two-Step Local Oxidation

In photosynthetic cells of *Rba. Sphaeroides*, the storage of solar energy starts with absorption of light by secondary LH2 antenna complexes, followed by energy transfer to the primary LH1 antenna, which surround and donate energy to the reaction center complexes, where the excitation energy is trapped and transformed into chemical energy.[1–3] These processes take place in membrane vesicles, 50–60 nm in diameter; to mimic this process on a silicon surface, groups of two types of photosynthetic complex must be patterned in close proximity (less than 5 nm intermolecular distance) to ensure efficient excitation energy transfer. We adapted the local oxidation nanopatterning protocol developed for a single type of light-harvesting proteins, i.e., RCLH1, LH2, and LHCII, to allow a successive local oxidation patterning and protein immobilization steps that would form a combined RCLH1 and LH2 nanopattern over the same area on the substrate (Figure 1B). In the first step, RCLH1 complexes were immobilized on four −COOH nanolines formed by the first AFM scan of the functionalized surface. After the immobilization of the RCLH1 complexes, a second scan was performed over the same area but at 90° with respect to the RCLH1 lines, creating three −COOH lines for the attachment of LH2 complexes.

The AFM topographic images in **Figure 6** show the RCLH1 and LH2 complexes immobilized on a silicon surface, where both the RCLH1 and LH2 nanolines are 10 µm in length (Figure 6A). Zooming in (yellow rectangle in Figure 6A) reveals the detailed topology of the crossover region (Figure 6B). It can be clearly seen that the RCLH1 lines are intersected by the LH2 lines, indicating that the original RCLH1 complexes were replaced by the LH2 complexes in the second nanopatterning step. A topographic cross section marked with the white dashed line in Figure 6B is plotted in Figure 6C. The RCLH1 lines are around 10 nm in height while the LH2 lines are about 7 nm in height, with an average FWHM of the LH2 and RCLH1 lines of ≈170 and ≈320 nm, respectively.

2.4. Investigating the Excitation Energy Transfer between Intersecting LH2 and RCLH1 Nanopatterns

The fluorescence signal from the crosspatterned lH2 and RCLH1 protein complexes was too weak for reliable data acquisition, because of the nonradiative substrate quenching of the fluorescence signal, and also because the high refractive index of the silicon substrate causes refraction of a substantial proportion of the emitted light that propagates within the evanescent field into the substrate. Our measurements were also hindered by the fact that the intersecting LH2 and RCLH1 nanolines have a limited contact interface at the intersections (where the two proteins are close enough for the excitation energy

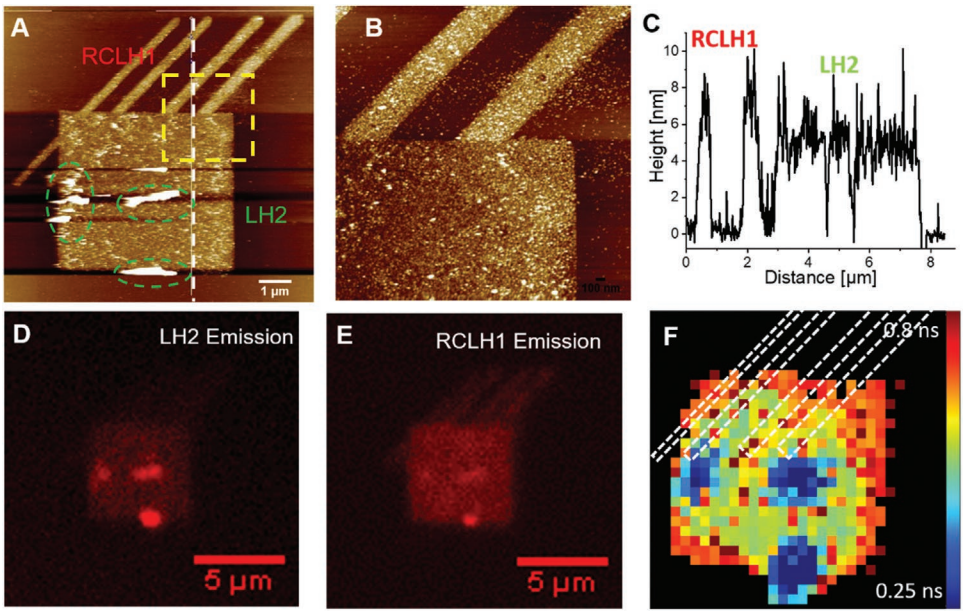

Figure 7. Characterization of a copatterned square array of LH2 complexes and RCLH1 nanolines. A) Topographic image of the square pattern with immobilized LH2 complexes and four intersection RCLH1 nanolines. B) Higher resolution zoom within the yellow dashed square in panel (A). C) Cross section along the white dashed line in panel (A), showing the height of the immobilized LH2 and RCLH1 complexes (6 and 8 nm, respectively). D,E) Wide-field fluorescence images recorded through 857/30 nm (LH2 emission) and 900/32 nm (RCLH1 emission) bandpass filters, respectively. F) Fluorescence lifetime image recorded at 857/ 3 nm (485 nm pulse laser excitation) showing the LH2 lifetime distribution within the square pattern with the position of the intersecting RCLH1 nanolines indicated by the dashed rectangles.

transfer to occur). These factors prevented the reliable detection of any significant changes in the LH2 fluorescence lifetime. Therefore, a larger area of LH2 was patterned in the shape of a 5 × 5 µm square. Four RCLH1 nanolines, 10 µm long, were fabricated partially intersecting the LH2 square pattern in order to increase the contact interface between the two protein complexes (see Figure S3 in the Supporting Information).

The sample was then characterized by AFM in order to evaluate the LH2 and RCLH1 distribution on the sample surface (**Figure** 7A,B), clearly showing that the protein complexes form a closely packed monolayer onto the silicon substrate. The height profile along the white dashed line (Figure 7C) shows that the RCLH1 nanolines are about 8 nm in height, while the LH2 square is about 6 nm in height (red and green dashed lines in Figure 7C, respectively). Some large aggregates, between 30 and 80 nm in height, appeared over the LH2 square pattern (Figure 7A, green ovals) after the RCLH1 immobilization (not present after the LH2 immobilization, see Figure S3 in the Supporting Information), indicating that these are likely to be RCLH1 aggregates.

The two-component LH2 / RCLH1 nanopattern was further analyzed by fluorescence lifetime imaging microscopy (FLIM) to investigate the retained functionality of the immobilized protein complexes and the ability of the LH2 antenna complexes to transfer excitation energy to the RCLH1 complexes. False color wide-field fluorescence images, shown in Figure 7D,E, were recorded in the LH2 and RCLH1 emission bands, respectively. The broad selectivity of the bandpass filters used (857/30 and 900/32 nm for LH2 and RCLH1 emissions, respectively) led to a significant crosstalk between the LH2 and RCLH1 signals, which were rather weak despite the increased detector sensitivity we employed. Thus, the fluorescence lifetime of the LH2 complexes was used as an indicator of possible excitation energy transfer to RCLH1 acceptors, which would be manifested as a significant decrease in the LH2 lifetime. It is worth noting that our home-built FLIM setup allows much better wavelength selection in lifetime imaging mode, i.e., 857 ± 3 nm for the LH2 emission. The intersection regions (white dashed boxes in Figure 7F), where the LH2 and RCLH1 complexes are in close proximity, however, did not exhibit significantly shorter lifetimes compared to the LH2-only parts of the pattern, with typical lifetimes of 0.5–0.7 ns (for example, along the right-hand side or the lower left corner of the square). On the other hand, the presence of RCLH1 aggregates on top of the LH2 square pattern (green ovals in Figure 7A) has clearly quenched the LH2 emission shortening the LH2 lifetime down to around 0.3 ns. We interpret this as a possible indication of energy transfer between the two types of complexes when they sit on top of each other, thus providing larger interface area.

Research on surface immobilization and patterning has been performed mostly on a single type of photosynthetic complex such as LH2, RCLH1, or LHCII on nonconductive surfaces like glass,[12–14] or conductive surfaces such as gold or ITO.[15–18] In all cases, the function of the complexes, for instance, the fluorescence emission, was retained. For example, surface-immobilized LHCII showed the ability to switch between fluorescent and quenched states,[14] while 80 nm wide nanolines of LH2 complexes exhibited long-range energy propagation on a micrometer scale, which greatly exceeds the natural energy propagation lengths of 50–100 nm within the native photosynthetic membranes.[30]

However, energy transfer in photosynthesis generally involves more than one type of complex, so nanoarrays of two or more types of photosynthetic complexes would be valuable tools to investigate biological light-harvesting and energy-transfer processes. Previous studies on simultaneous patterning of two or more types of protein complexes on the same surface focused on the fabrication process itself and the functional state of immobilized assemblies,[14,55] while only our very recent work went on to investigate the excitation energy transfer occurring between LH2 and RCLH1 patterned on micrometer scale onto glass substrate.[38]

Here, we have employed a simple lithographic method that allowed us to pattern two or more photosynthetic complexes on a conductive surface, with their distribution controlled on the nanometer scale for studying the processes of light harvesting and energy transfer. The most efficient experimental conditions have been found for mPEG molecule's oxidation and protein immobilization, and at the points of intersection of the copatterns we found some evidence for shortened lifetimes of LH2 energy donor complexes, where they are in proximity to RCLH1 acceptor complexes.

Previous studies have shown that larger bias value and longer probe dwell times generally contribute to more efficient mPEG oxidation;[40] we have found the optimal conditions for local oxidation in our system, and further increases in the probe bias and dwell time impair protein attachment. For example, when applying a probe–sample bias of 12 V, increasing the dwell time above 100 ms pixel^{-1} (at a pixel density of 25.6 pixels μm^{-1}) does not lead to further oxidation of the mPEG monolayer. It is possible that the oxidation of the underlying silicon on the substrate surface produces a swollen layer of nonconductive SiO_2, which reduces the electric field strength as the oxide thickness increases,[43] preventing further oxidation of mEPG. At 12 V of bias voltage and 100 ms pixel^{-1} dwell time, the oxide thickness was found to be ≈1 nm; taking into account the native 2.5 nm oxide layer, the total thickness of the SiO_2 on the surface is likely to be 3.5 nm. Previous local oxidation experiments reported that the thickness of SiO_2 stays below 5 nm, and a swelling to 8 nm was reported only in some extreme cases.[56–59] Therefore, we can conclude that our experimental conditions, bias of 12 V and 100 ms per dwell time, were optimal for the oxidation of the mPEG functional monolayer.

Many studies have shown that photosystem complexes retain their function when immobilized on different conductive surfaces, such as bacterial RCs on ITO-coated glass,[60] gold electrodes,[61–63] or gallium arsenide;[64] and photosystem II[65–67] and photosystem I[68–70] on electrodes. However, no previous research reports simultaneous nanopatterning of two different photosynthetic complexes on a conductive surface while retaining functionality of each protein component.

We attempted to impose a second protein pattern on an existing array, by writing lines of RCLH1 into a square assembly of tightly packed LH2 complexes (Figure 7). The difference of 1–2 nm in the measured heights along the surface profiles displayed in Figures 6C and 7C is likely due to packing constraints lifting some of the protein complexes slightly off the substrate, resulting in some height variation along the patterned lines, as clearly visible in Figure 6B. In this case, it is likely that the limited scope for further surface oxidation and the very high occupancy of LH2 complexes did not allow deposition of many RCLH1 complexes among the existing LH2 proteins. In addition to that, the areas where the RCH1 nanolines intersect the LH2 square the interface area between the two proteins is probably too small, which, combined with the weak signal due to the substrate quenching, limits the ability of our experimental set up to distinguish between the quenched and non-quenched LH2 complexes. Thus, we only see some evidence for LH2-to-RCLH1 excitation energy transfer in the areas where RCLH1 aggregates were deposited unintentionally on top of the LH2 square; the evidence for energy transfer rests on the variation in the fluorescence lifetime of the LH2 complexes (Figure 7F). Overall, an interplay of several factors hindered the lifetime measurements—substrate quenching of the fluorescence emission signal together with the relatively small number of protein complexes participating in the energy transfer process (only those sitting at the interface between the two proteins), resulted in somewhat limited evidence for energy transfer from LH2 to RCLH1.

However, the AFM topographic images of the copatterned RCLH1 and LH2 nanolines unequivocally show that the two proteins co-exist within the same area on the substrate (Figures 6 and 7A), while the acquired fluorescence emission spectra clearly demonstrate the retained structural and optical properties of the protein complexes.

We envisage that immobilizing light-harvesting proteins onto a conductive substrate can be beneficial when studying their electrical properties. In fact, the RCLH1 function within the photosynthetic membrane is not only to gather light, but also to perform the electrochemical charge separation (in the reaction center). Previous studies have already demonstrated the usefulness of LH2 or RCLH1 proteins randomly immobilized onto conductive substrates (metals) to study their electrical properties and their potential applications in biohybrid devices and biosensors.[15,18,20,21,71,72] Thus, our method for a precise immobilization of multiple light-harvesting proteins on the nanoscale onto a semiconductive substrate that is widely used in microelectronics and nanofabrication (silicon wafers) is highly relevant when investigating future biohybrid and biophotovoltaic applications of the light-harvesting proteins.

3. Conclusion

In this work, we have demonstrated that photosynthetic protein complexes can be patterned on semiconductive silicon surface on the nanometer scale with high protein occupancy of the nanopatterned areas. We deliberately chose the silicon over the widely used glass because of its semiconductivity, which allowed us to employ a conductive local oxidation patterning method that permits very specific spatial placement of the protein complexes. However, the high refractive index of the silicon substrate together with a nonradiative quenching of the sample's fluorescence hindered full investigation of the energy-transfer functionality of the light-harvesting proteins used in this study. Future work where a transparent conductive substrate is used (such as ITO) might be able to overcome this limitation. In addition, conductive substrates would allow us to investigate the electrical properties of such multicomponent

protein nanoassemblies by employing conductive scanning probe methods to quantify the photocurrent generated by the RCLH1 complexes. We also envisage that such two-component nanopatterns might be ideal model systems to study the electrical properties of RC complexes and their role in the energy transfer and charge separation at nanoscale or single-molecule level.

4. Experimental Section

Protein Purification: Wild-type LH2 and RCLH1 proteins were purified as described previously.[73,74] Briefly, semiaerobically grown cells were harvested and disrupted in a French pressure cell at 18 000 psi. After centrifugation, the supernatant was loaded onto a sucrose gradient in order to isolate the ICM. After harvesting, the ICMs were solubilized in 3% (v/v) β-DDM for RCLH1 and in 4% (v/v) *N*,*N*-dimethyldodecylamine-*N*-oxide (LDAO) for LH2 by stirring in the dark at 4 °C for 45 min. The solubilized membrane solution was diluted at least threefold in working buffer containing 10×10^{-3} M HEPES, pH 7.8, 50×10^{-3} M NaCl, and 0.03% (w/v) β-DDM. After that, the solubilized material was centrifuged for 1 h in a Beckman Ti 70.1 rotor at 48 000 rpm (160 000 × *g*) at 4 °C to remove insolubilized material. The supernatant was further purified by using ion-exchange chromatography and concentrated using Amicon 100 000 MWCO spin filters (Millipore) in 10×10^{-3} M HEPES, pH 7.8, 50×10^{-3} M NaCl, and 0.03% (w/v) β-DDM buffer.

Wild-type trimeric LHCII protein was purified from spinach leaves as described previously[75] with some modifications. Briefly, spinach leaves were blended and filtered in 1:1 (v/w) ice-cold buffer (50×10^{-3} M Na_3PO_4, pH 7.4, 5×10^{-3} M $MgCl_2$, 300×10^{-3} M sucrose). The pellet was resuspended and centrifuged in osmotic buffer (10×10^{-3} M Tricine, pH 7.4, 5×10^{-3} M $MgCl_2$, 200×10^{-3} M sucrose) to yield pelleted thylakoids. After harvesting, the thylakoids were digested in *n*-dodecyl α-maltoside (α-DDM), and unbroken thylakoids were removed by centrifugation at 1000 × *g* for 5 min. The supernatant was further purified by sucrose gradient sedimentation (8–14% sucrose, centrifugation at 100 000 × *g* for 36 h at 4 °C), and the trimeric LHCII was purified by subsequent high-resolution size-exclusion fast protein liquid chromatography (AKTA).

Sample Preparation: Silicon wafers with native oxide layer, p-type (boron)-doped [1 0 0] (Siegert wafer), were used as substrates. Silicon substrates and glass vials were cleaned by immersion for 40 min in a piranha solution consisting of 30% hydrogen peroxide (Fisher Scientific) and 95% sulfuric acid (Fisher Scientific) at a ratio of 3:7. A self-assembled monolayer of mPEG-terminated silane (mPEG-SAM) was formed by immersing the silicon substrate in a solution of 15×10^{-3} M 2-[methoxy(polyethyleneoxy)6-9propyl] trichlorosilane (mPEG chlorosilane) (Gelest) in 99.8% anhydrous toluene (Sigma–Aldrich) for 2 h. The mPEG-SAM-coated silicon was rinsed thoroughly with toluene and acetone then dried under a stream of argon.

The oxidation patterning was performed on the mPEG-SAM-coated substrate, using AFM (Multimode 8, Bruker) in contact mode in air at a relative humidity of ≈40%. A conductive AFM probe (Bruker, CONTV-PT), coated by a Pt–Ir layer, was scanned over the substrate with a voltage bias, locally oxidizing the $-CH_3$ groups on the mPEG to $-COOH$ groups.[34–36] The raster scan pixel resolution was at 256 pixels over 10 µm scan size (25.6 pixel µm^{-1}) for nanolines and 256 pixels over 5 µm scan size (51.2 pixel µm^{-1}) for the 5×5 µm^2 square pattern. After the local oxidations step, the substrates were treated with 20×10^{-3} M EDC (Thermo Scientific) and 20×10^{-3} M NHS (Thermo Scientific) for 1 h at pH 5.8 to form NHS ester over the oxidized areas for protein immobilization.

The substrate with amine-reactive NHS ester was immersed in a protein solution (2×10^{-6} M protein in buffer consisting of 20×10^{-3} M HEPES, 0.03% w/v β-DDM, pH 7.4) for protein immobilization. Then, the sample was rinsed three times by detergent buffer (20×10^{-3} M HEPES, 0.03% w/v β-DDM, pH 7.4) to remove weakly binding proteins. Samples were then imaged by the AFM in buffer (20×10^{-3} M HEPES, 20×10^{-3} M NaCl, 5×10^{-3} M $MgCl_2$) for the topography and by FLIM in buffer (20×10^{-3} M HEPES, 0.03% w/v β-DDM) for optical properties and for energy transfer studies.

Atomic Force Microscopy Imaging: The AFM data were collected on a Multimode 8 instrument coupled to a NanoScope V controller (Bruker). NanoScope software (v8.15, Bruker) was used for data collection. Gwyddion (v2.52, open source software, www.gwyddion.net), OriginPro (v8.5.1, OriginLab Corp.), and ImageJ (open source) were used for data processing and analysis.

Topography and lateral force images of the local oxidation patterns were recorded in contact mode in air immediately following the oxidation-patterning process by a conductive AFM probe (Bruker, CONTV-PT) coated by a Pt–Ir layer. Protein patterns were imaged in peak-force tapping mode in imaging buffer (20×10^{-3} M HEPES, 20×10^{-3} M NaCl, pH 7.8) using "SNL-10" probes (56 kHz, $k \approx 0.24$ N m^{-1}) (Bruker Nano). The peak-force amplitude was 10 nm and images were taken using 256 × 256 or 512 × 512 pixel arrays. The peak-force set point varied between 50 and 1000 pN, and the scan rate was between 0.5 and 1.0 Hz.

Fluorescence Lifetime Imaging Microscopy: The fluorescence emission properties of samples were measured on a home-built time-resolved fluorescence microscope. The microscope was equipped with two different light sources: a 470 nm light-emitting diode (LED; Thorlabs, M470L2) for spectral measurement and wide-field fluorescence images; and a 485 nm picosecond diode laser (PicoQuant, PDL 828) for lifetime measurements. The excitation light was focused by a 100× objective (PlaneFluorite, numerical aperture = 1.4, oil immersion, Olympus) and the fluorescence emission was collected from the same focal spot on the sample. The collected light was then filtered by a 495 nm dichroic beam-splitters (Semrock) to remove the background excitation light. An 857/30 nm bandpass filter was used for the LH2 imaging and a 900/32 nm bandpass filter for the RCLH1 imaging. An imaging spectrometer (Acton SP2558, Princeton Instruments) fitted with an electron-multiplying CCD(EMCCD) detector (ProEM 512, Princeton Instruments) and a hybrid detector (HPM-100-50, Becker & Hickl) allowed simultaneous spectral and lifetime imaging. Samples were excited by the 485 nm pulsed laser at 1 MHz repetition rate and a fluence of $\approx 2 \times 10^{14}$ photons pulse^{-1} cm^{-2}, and the modulation of the laser was synchronized with a time-correlated single-photon counting (TCSPC) module (SPC-150, Becker & Hickl) for the lifetime decay measurement. During the measurement, the entrance slit of the spectrometer was closed to 100 µm. A grating with 150 lines mm^{-1} was used to select the wavelength. A secondary exit slit on the spectrometer was used to narrow the recording wavelength range to 3 nm.

Wide-field fluorescence images were analyzed by Image J; the spectral data were analyzed in OriginPro; and the fluorescence decay curves were analyzed in OriginPro and TRI2 (open source), with fitting using the multiexponential decay function

$$I(t) = A_1 \exp\left(\frac{-t}{\tau_1}\right) + A_2 \exp\left(\frac{-t}{\tau_2}\right) + B \tag{1}$$

where τ is the fluorescence lifetime, A is the fractional amplitude contribution of the decay component, and B is the background. The quality of the fit was judged on the basis of the reduced χ^2 statistic

$$\chi^2_{\text{red}} = \frac{\sum_{k=1}^{n} \frac{\left[I(t_k) - I_c(t_k)\right]^2}{I(t_k)}}{n-p} = \frac{\chi^2}{n-p} \tag{2}$$

where t_k is the time point k, $I(t_k)$ is the data at the time point k, $I_c(t_k)$ is the fit at the time point k, n is the number of the data points, and p is the number of the variable fit parameters ($n - p$ = degrees of freedom).

Using a mirror to replace the sample, the time delay of the laser from the pulse starting point to the instrument responding point was measured. Such a time delay was defined as the instrument response function (IRF), which was ≈130 ps on the home-built fluorescence microscope. The IRF was taken into account when the fitting was performed for the decay curves.

Supporting Information

Supporting Information is available from the Wiley Online Library or from the author.

Acknowledgements

This work was supported as part of the Photosynthetic Antenna Research Center (PARC), an Energy Frontier Research Center funded by the U.S. Department of Energy, Office of Science, Basic Energy Sciences program under Award Number DE-SC0001035. PARC supported the AFM, spectral imaging, and fluorescence lifetime studies, provided a doctoral studentship for X.H., supported C.V. and provided partial support for C.N.H. C.N.H. also acknowledges financial support from the Biotechnology and Biological Sciences Research Council (BBSRC UK), Award Number BB/M000265/1, and European Research Council Synergy Award 854126.

Conflict of Interest

The authors declare no conflict of interest.

Author Contributions

Conceptualization: X.H., C.N.H., and C.V. Data curation and formal analysis: C.V. and X.H. Funding acquisition: C.N.H. Investigation: X.H. and C.V. Methodology: C.V. and C.N.H. Project administration and resources: C.N.H. Supervision: C.V. and C.N.H. Writing original draft: X.H., C.V., and C.N.H. Writing review and editing: C.V. and C.N.H.

Keywords

atomic force microscopy, light-harvesting proteins, nanopatterning, scanning probe lithography

Received: September 23, 2020
Revised: November 25, 2020
Published online:

[1] M. Sener, J. Strümpfer, S. Abhishek, C. N. Hunter, K. Schulten, *eLife* **2016**, *5*, e09541.
[2] P. D. Dahlberg, P.-C. Ting, S. C. Massey, M. A. Allodi, E. C. Martin, C. N. Hunter, G. S. Engel, *Nat. Commun.* **2017**, *8*, 988.
[3] A. Singharoy, C. Maffeo, K. H. Delgado-Magnero, D. J. K. Swainsbury, M. Sener, U. Kleinekathöfer, J. E. Vant, J. Nguyen, A. Hitchcock, B. Isralewitz, I. Teo, D. Chandler, J. Stone, J. Phillips, T. V. Pogorelov, M. I. Mallus, C. Chipot, Z. Luthey-Schulten, P. Tieleman, C. N. Hunter, E. Tajkhorshid, A. Aksimentiev, K. Schulten, *Cell* **2019**, *179*, 1098.
[4] J. D. Tucker, C. A. Siebert, M. Escalante, P. G. Adams, J. D. Olsen, C. Otto, D. L. Stokes, C. N. Hunter, *Mol. Microbiol.* **2010**, *76*, 833.
[5] P. G. Adams, C. N. Hunter, *Biochim. Biophys. Acta, Bioenerg.* **2012**, *1817*, 1616.
[6] M. K. Şener, J. D. Olsen, C. N. Hunter, K. Schulten, *Proc. Natl. Acad. Sci. USA* **2007**, *104*, 15723.
[7] M. K. Şener, K. Schulten, in *The Purple Phototrophic Bacteria* (Eds: C. N. Hunter, F. Daldal, M. C. Thurnauer, J. T. Beatty), Springer, Dordrecht, Netherlands **2009**, pp. 275–294.
[8] R. G. Nuzzo, D. L. Allara, *J. Am. Chem. Soc.* **1983**, *105*, 4481.
[9] E. Delamarche, B. Michel, H. A. Biebuyck, C. Gerber, *Adv. Mater.* **1996**, *8*, 719.
[10] A. Ulman, *Chem. Rev.* **1996**, *96*, 1533.
[11] K. Wen, R. Maoz, H. Cohen, J. Sagiv, A. Gibaud, A. Desert, B. M. Ocko, *ACS Nano* **2008**, *2*, 579.
[12] M. Escalante, P. Maury, C. M. Bruinink, K. van der Werf, J. D. Olsen, J. A. Timney, J. Huskens, C. N. Hunter, V. Subramaniam, C. Otto, *Nanotechnology* **2008**, *19*, 025101.
[13] M. Escalante, Y. Zhao, M. J. Ludden, R. Vermeij, J. D. Olsen, E. Berenschot, C. N. Hunter, J. Huskens, V. Subramaniam, C. Otto, *J. Am. Chem. Soc.* **2008**, *130*, 8892.
[14] C. Vasilev, M. P. Johnson, E. Gonzales, L. Wang, A. V. Ruban, G. Montano, A. J. Cadby, C. N. Hunter, *Langmuir* **2014**, *30*, 8481.
[15] M. Kondo, Y. Nakamura, K. Fujii, M. Nagata, Y. Suemori, T. Dewa, K. Iida, A. T. Gardiner, R. J. Cogdell, M. Nango, *Biomacromolecules* **2007**, *8*, 2457.
[16] N. P. Reynolds, S. Janusz, R. E. Ducker, G. J. Leggett, M. Escalante-Marun, J. Timney, R. E. Ducker, J. D. Olsen, C. Otto, V. Subramaniam, G. J. Leggett, C. N. Hunter, *J. Am. Chem. Soc.* **2007**, *129*, 14625.
[17] S. Patole, C. Vasilev, O. El-Zubir, L. Wang, M. P. Johnson, A. J. Cadby, G. J. Leggett, C. N. Hunter, *Interface Focus* **2015**, *5*, 20150005.
[18] Y. Suemori, M. Nagata, Y. Nakamura, K. Nakagawa, A. Okuda, J.-I. Inagaki, K. Shinohara, M. Ogawa, K. Iida, T. Dewa, K. Yamashita, A. Gardiner, R. J. Cogdell, M. Nango, *Photosynth. Res.* **2006**, *90*, 17.
[19] S. C. Tan, L. I. Crouch, S. Mahajan, M. R. Jones, M. E. Welland, *ACS Nano* **2012**, *6*, 9103.
[20] M. Kamran, J. D. Delgado, V. Friebe, T. J. Aartsma, R. N. Frese, *Biomacromolecules* **2014**, *15*, 2833.
[21] M. Kamran, V. M. Friebe, J. D. Delgado, T. J. Aartsma, R. N. Frese, M. R. Jones, *Nat. Commun.* **2015**, *6*, 6530.
[22] G. J. Leggett, *Nanoscale* **2012**, *4*, 1840.
[23] H. Sorribas, C. Padeste, L. Tiefenauer, *Biomaterials* **2002**, *23*, 893.
[24] N. P. Reynolds, J. D. Tucker, P. A. Davison, J. A. Timney, C. N. Hunter, G. J. Leggett, *J. Am. Chem. Soc.* **2009**, *131*, 896.
[25] S. Xia, M. Cartron, J. Morby, D. A. Bryant, C. N. Hunter, G. J. Leggett, *Langmuir* **2016**, *32*, 1818.
[26] K. B. Lee, S. J. Park, C. A. Mirkin, J. C. Smith, M. Mrksich, *Science* **2002**, *295*, 1702.
[27] K.-B. Lee, J.-H. Lim, C. A. Mirkin, *J. Am. Chem. Soc.* **2003**, *125*, 5588.
[28] M. Lee, D.-K. Kang, H.-K. Yang, K.-H. Park, S. Y. Choe, C. S. Kang, S.-I. Chang, M. H. Han, I.-C. Kang, *Proteomics* **2006**, *6*, 1094.
[29] S. W. Lee, B. K. Oh, R. G. Sanedrin, K. Salaita, T. Fujigaya, C. A. Mirkin, *Adv. Mater.* **2006**, *18*, 1133.
[30] M. Escalante, A. Lenferink, Y. Zhao, N. Tas, J. Huskens, C. N. Hunter, V. Subramaniam, C. Otto, *Nano Lett.* **2010**, *10*, 1450.
[31] S. Sun, G. J. Leggett, *Nano Lett.* **2004**, *4*, 1381.
[32] S. Sun, M. Montague, K. Critchley, M.-S. Chen, W. J. Dressick, S. D. Evans, G. J. Leggett, *Nano Lett.* **2006**, *6*, 29.
[33] E. Ul-Haq, S. Patole, M. Moxey, E. Amstad, C. Vasilev, C. N. Hunter, G. J. Leggett, N. D. Spencer, N. H. Williams, *ACS Nano* **2013**, *7*, 7610.
[34] R. Maoz, E. Frydman, S. R. Cohen, J. Sagiv, *Adv. Mater.* **2000**, *12*, 424.
[35] R. Maoz, E. Frydman, S. R. Cohen, J. Sagiv, *Adv. Mater.* **2000**, *12*, 725.
[36] I. Choi, S. K. Kang, J. Lee, Y. Kim, J. Yi, *Biomaterials* **2006**, *27*, 4655.
[37] I. Choi, S. K. Kang, J. Lee, Y. Kim, J. Yi, *Sens. Actuators, B* **2008**, *129*, 734.
[38] X. Huang, C. Vasilev, C. N. Hunter, *Lab Chip* **2020**, *20*, 2529.
[39] S. Hoeppener, R. Maoz, S. R. Cohen, L. F. Chi, H. Fuchs, J. Sagiv, *Adv. Mater.* **2002**, *14*, 1036.
[40] D. Wouters, R. Willems, S. Hoeppener, C. F. J. Flipse, U. S. Schubert, *Adv. Funct. Mater.* **2005**, *15*, 938.

[41] M. Yang, D. Wouters, M. Giesbers, U. S. Schubert, H. Zuilhof, *ACS Nano* **2009**, *3*, 2887.
[42] S. Krakert, N. Ballav, M. Zharnikov, A. Terfort, *Phys. Chem. Chem. Phys.* **2010**, *12*, 507.
[43] P. Avouris, T. Hertel, R. Martel, *Appl. Phys. Lett.* **1997**, *71*, 285.
[44] P. Qian, E. C. Martin, I. W. Ng, C. N. Hunter, *Biochim. Biophys. Acta* **2017**, *1858*, 795.
[45] P. Qian, M. Z. Papiz, P. J. Jackson, A. A. Brindley, I. W. Ng, J. D. Olsen, M. J. Dickman, P. A. Bullough, C. N. Hunter, *Biochemistry* **2013**, *52*, 7575.
[46] S. C. Chi, D. J. Mothersole, P. Dilbeck, D. M. Niedzwiedzki, H. Zhang, P. Qian, C. Vasilev, K. J. Grayson, P. J. Jackson, E. C. Martin Y. Li, D. Holten, C. N. Hunter, *Biochim. Biophys. Acta* **2015**, *1847*, 189.
[47] J. D. Olsen, J. D. Tucker, J. A. Timney, P. Qian, C. Vasilev, C. N. Hunter, *J. Biol. Chem.* **2008**, *283*, 30772.
[48] S. Kumar, M. L. Cartron, N. Mullin, P. Qian, G. J. Leggett, C. N. Hunter, J. K. Hobbs, *ACS Nano* **2017**, *11*, 126.
[49] M. Z. Papiz, S. M. Prince, T. Howard, R. J. Cogdell, N. W. Isaacs, *J. Mol. Biol.* **2003**, *326*, 1523.
[50] P. G. Adams, C. N. Hunter, *Biochim. Biophys. Acta* **2012**, *1817*, 1616.
[51] Z. Liu, H. Yan, K. Wang, T. Kuang, J. Zhang, L. Gul, X. An, W. Chang, *Nature* **2004**, *428*, 287.
[52] J. J. Standfuss, A. C. Terwisscha van Scheltinga, M. Lamborghini, W. Kuhlbrandt, *EMBO J.* **2005**, *24*, 919.
[53] H. Khun, *J. Chem. Phys.* **1970**, *53*, 101.
[54] L. Danos, R. Greef, T. Markvart, *Thin Solid Films* **2008**, *516*, 7251.
[55] O. El Zubir, S. Xia, R. E. Ducker, L. Wang, N. Mullin, M. L. Cartron, A. J. Cadby, J. K. Hobbs, C. N. Hunter, G. J. Leggett, *Langmuir* **2017**, *33*, 8829.
[56] P. A. Fontaine, E. Dubois, D. Stiévenard, *J. Appl. Phys.* **1998**, *84*, 1776.
[57] T.-H. Fang, *Microelectron. J.* **2004**, *35*, 701.
[58] M. Yang, Z. Zheng, Y. Liu, B. Zhang, *Nanotechnology* **2005**, *17*, 330.
[59] M. Yang, Z. Zheng, Y. Liu, B. Zhang, *J. Phys. Chem. B* **2006**, *110*, 10365.
[60] R. Das, P. J. Kiley, M. Segal, J. Norville, A. A. Yu, L. Wang, S. A. Trammell, L. E. Reddick, R. Kumar, F. Stellacci, N. Lebedev, J. Schnur, B. D. Bruce, S. Zhang, M. Baldo, *Nano Lett.* **2004**, *4*, 1079.
[61] J. Zhao, Y. Zou, B. Liu, C. Xu, J. Kong, *Biosens. Bioelectron.* **2002**, *17*, 711.
[62] S. A. Trammell, I. Griva, A. Spano, S. Tsoi, L. M. Tender, J. Schnur, N. Lebedev, *J. Phys. Chem. C* **2007**, *111*, 17122.
[63] M.-H. Ham, J. H. Choi, A. A. Boghossian, E. S. Jeng, R. A. Graff, D. A. Heller, A. C. Chang, A. Mattis, T. H. Bayburt, Y. V. Grinkova, A. S. Zeiger, K. J. Van Vliet, E. K. Hobbie, S. G. Sligar, C. A. Wraight, M. S. Strano, *Nat. Chem.* **2010**, *2*, 929.
[64] L. Frolov, Y. Rosenwaks, S. Richter, C. Carmeli, I. Carmeli, *J. Phys. Chem. C* **2008**, *112*, 13426.
[65] A. Badura, B. Esper, K. Ataka, C. Grunwald, C. Wöll, J. Kuhlmann, J. Heberle, M. Rögner, *Photochem. Photobiol.* **2006**, *82*, 1385.
[66] M.-J. den Hollander, J. G. Magis, P. Fuchsenberger, T. J. Aartsma, M. R. Jones, R. N. Frese, *Langmuir* **2011**, *27*, 10282.
[67] N. Terasaki, M. Iwai, N. Yamamoto, T. Hiraga, S. Yamada, Y. Inoue, *Thin Solid Films* **2008**, *516*, 2553.
[68] C. J. Faulkner, S. Lees, P. N. Ciesielski, D. E. Cliffel, G. K. Jennings, *Langmuir* **2008**, *24*, 8409.
[69] H. Krassen, A. Schwarze, B. Friedrich Br, K. Ataka, O. Lenz, J. Heberle, *ACS Nano* **2009**, *3*, 4055.
[70] O. Yehezkeli, O. I. Wilner, R. Tel-Vered, D. Roizman-Sade, R. Nechushtai, I. Willner, *J. Phys. Chem. B* **2010**, *114*, 14383.
[71] V. M. Friebe, R. N. Frese, *Curr. Opin. Electrochem.* **2017**, *5*, 126.
[72] J. Liu, V. M. Friebe, R. N. Frese, M. R. Jones, *Nat. Commun.* **2020**, *11*, 1.
[73] P. Qian, C. N. Hunter, P. A. Bullough, *J. Mol. Biol.* **2005**, *349*, 948.
[74] T. Walz, S. J. Jamieson, C. M. Bowers, P. A. Bullough, C. N. Hunter, *J. Mol. Biol.* **1998**, *282*, 833.
[75] A. V. Ruban, A. J. Young, A. A. Pascal, P. Horton, *Plant Physiol.* **1994**, *104*, 227.